Transformation of polymer-ZnO core–shell nanofibers into ZnO hollow nanofibers: Intrinsic defect reorganization in ZnO and its influence on the photocatalysis

Fatma Kayaci [a,b], Sesha Vempati [a,*], Cagla Ozgit-Akgun [a,b], Inci Donmez [a,b], Necmi Biyikli [a,b], Tamer Uyar [a,b,**]

[a] UNAM-National Nanotechnology Research Center, Bilkent University, Ankara 06800, Turkey
[b] Institute of Materials Science and Nanotechnology, Bilkent University, Ankara 06800, Turkey

ABSTRACT

Photocatalytic activity (PCA) on semiconductors is known to be majorly influenced by specific surface area and intrinsic lattice defects of the catalyst. In this report, we tested the efficiencies of 1D ZnO catalysts of varying fiber diameter (80 nm and 650 nm of inner diameter) in two formats, viz. core–shell and hollow nanofibers, where the former is calcined to yield the latter. These nanofibrous catalysts were produced by combining electrospinning and atomic layer deposition processes which were then subjected to thorough characterization including photoluminescence (PL) unveiling the details of intrinsic defects/densities. During the thermal treatment, intrinsic defects are reorganized and as a result a new PL band is observed apart from some significant changes in the intensities of other emissions. The densities of various intrinsic defects from PL are compared for all samples and juxtaposed with the PCA. Careful scrutiny of the various results suggested an anti-correlation between surface area and PCA; i.e., higher surface area does not necessarily imply better PCA. Beyond a limit, the most deterministic factor would be the density of surface defects rather than the specific surface area. The results of this study enable the researchers to fabricate 1D semiconductor photocatalysts while striking the balance between surface area and density of defects.

© 2015 Elsevier B.V. All rights reserved.

1. Introduction

Ever increasing environmental pollution forces the researchers to fabricate efficient catalysts which can use sunlight to disintegrate or oxidize the organic substances [1–14]. It is known that delaying the recombination of photogenerated electron–hole pair increases the efficiency of the catalysts [10,12,15–23]. On the other hand, the efficiency of the catalyst is dependent on the crystal-phase [1,3]. i.e., the formation of $^\bullet$OH radical [12–14] depends on the crystalline facets those were exposed. Moreover, researchers have attempted to increase the surface area to volume ratio. This not only minimizes the usage of catalyst but also enhances the active sites on the surface [10–13,18]. One should note that other significant attempts of enhancing the photocatalytic activity (PCA) or

delaying the recombination are lattice defects [12,16,18–23], heterojunctions [4,10,14–17,24–26] etc. It is also notable that PCA is a very complex process and it is an integral effect of surface sites, bulk of the lattice etc. [2]. Here we consider two factors which are interlinked; viz. surface area and density of defects in conjunction with thermal treatment [27]. To unveil the dependency of surface area and density of defects on PCA, we have chosen ZnO as a model semiconductor as it is vastly studied in the context of PCA [10,16,18,28–34]. While reducing the dimensions of the catalysts (increasing the specific surface area), an increase in the density of surface states is inevitable due to the dangling orbitals [35], in addition to intrinsic lattice defects [36]. ZnO is associated with defects such as zinc interstitials (Zn_i^{++}, Zn_i^+, Zn_i^*, extended-Zn_is (ex-Zn_is)), oxygen vacancies (V_O^{++}, V_O^+ and V_O) and zinc vacancies (V_{Zn}'', V_{Zn}' and V_{Zn}) [37,38]. Note that our interest is not to control the defect density, rather to understand how it changes when the specific surface area is increased via high temperature thermal treatment. Please refer to our earlier investigation in which we have elucidated the role of Zn_is and V_Os by carefully controlling their density [11]. In this article, we compare the relative densities

* Corresponding author. Tel.: +90 3122903533.
** Corresponding author at: UNAM-National Nanotechnology Research Center, Bilkent University, Ankara 06800, Turkey. Tel.: +90 3122903571.
   E-mail addresses: svempati01@qub.ac.uk (S. Vempati), tamer@unam.bilkent.edu.tr (T. Uyar).
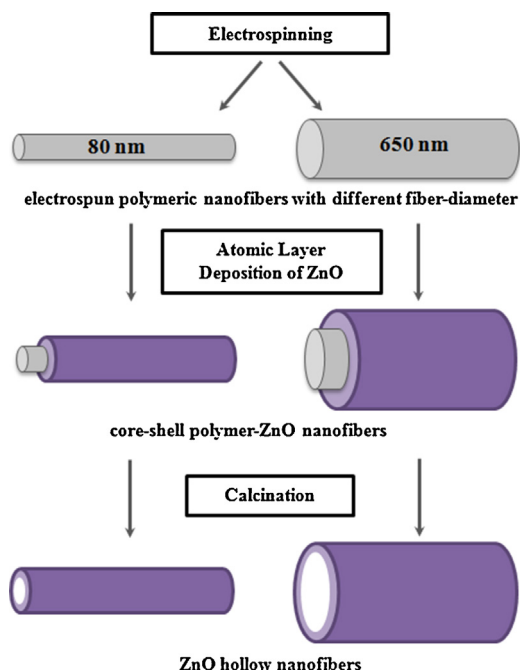
Fig. 1. Schematic diagram depicting the steps involved to produce core–shell and hollow nanofibers.

of some of the above listed intrinsic defects with reference to the calcination effect and PCA. The catalysts examined here were fabricated via a renounced and industrially applicable combination [10,11,18,28,29,39–41], viz. electrospinning [42–44] and atomic layer deposition (ALD) [45–49].

Here we have produced nylon 6,6 nanofibers of two average diameters (80 nm and 650 nm) by electrospinning and applied ZnO nanocoating by ALD to produce polymer-ZnO core–shell nanofiber structure. We have extracted some results (X-ray diffraction and PCA) from core–shell structures [29] and compared it with the hollow counterpart, where the latter were produced by calcining the former. The calcination not only increases the surface area but also manipulates the relative densities of defects. We have systematically characterized these catalysts to understand the effects of calcination on the morphology, crystallinity, chemisorbed oxygen (O_{Ch}) and photoluminescence (PL). Note that the relative changes in the density of defects can be easily monitored through PL spectroscopy [10,11,18,36,50–52]. Interestingly, in the context of PL we have observed defect reorganization and a new emission from the ZnO hollow nanofibers. The results suggest that the excessive increase in the surface area cannot equivalently enhance the PCA and a careful balance against the surface area and defect density is required.

2. Experimental

2.1. Materials

Formic acid (FA, 98–100%) or 1,1,1,3,3,3-hexafluoro-2-propanol (HFIP, ≥99%) were used as solvents for nylon 6,6. Diethylzinc (DEZn) and HPLC grade water were used as the zinc precursor and oxidant, respectively. Rhodamine-B (Rh-B, dye content ~95%) was used as a model organic dye. All chemicals were used as received from Sigma–Aldrich while de-ionized (DI) water is obtained from Millipore Milli-Q system.

2.2. Electrospinning of nylon 6,6 nanofibers

Uniform and bead-free nylon 6,6 nanofibers with two different average fiber diameters were produced by varying the solvent system (FA or HFIP) based on our previous study [29]. Two solutions were prepared, viz. 8 wt.% nylon 6,6 in FA or HFIP. The two solutions were stirred for 3 h at room temperature to obtain a homogeneous and clear solution. Each of these solutions was taken in a syringe fitted with a metallic needle of ~0.8 mm of inner diameter. Then the syringe with solution was fixed horizontally on a syringe pump (KD Scientific, KDS 101) with a feed rate of 1 mL/h. A 15 kV high voltage is applied (Matsusada, AU Series) between the metal needle and a grounded electrode which was kept at a distance of ~10 cm. Grounded electrode was wrapped with an aluminium foil to collect the fibers. The electrospinning process was carried out at ~23 °C and 36% relative humidity in an enclosed chamber.

2.3. Core–shell to hollow ZnO nanofibers

The electrospun polymeric nanofibers were introduced into the ALD system (Savannah S100 ALD reactor, Cambridge Nanotech Inc.) and ZnO was deposited via a process similar to our previous study [29]. Briefly, the deposition was performed at ~200 °C with a growth per cycle of ~1.13 Å using N_2 as a carrier gas at a flow rate of 20 sccm. 800 cycles were applied and each cycle consisted of the following steps: DEZn pulse (0.015 s)/N_2 purge (10 s)/H_2O pulse (0.015 s)/N_2 purge (10 s). The resultant coating was ~90 nm thick forming a core–shell structure. After the deposition, the samples were calcined at 500 °C for 2 h under ambient atmosphere. This process essentially removed the core polymer and hollow ZnO nanofibers were formed. The average fiber diameter (AFD) of the pure nylon 6,6 nanofibers obtained from 8 wt.% nylon 6,6 in FA or HFIP were estimated to be 80 nm or 650 nm, respectively via analyzing scanning electron microscope (SEM) images [29]. For easy discussion, core–shell and hollow ZnO nanofibrous samples are referred as ^{CS}80 nm/^{CS}650 nm and ^{H}80 nm/^{H}650 nm, respectively. The estimated fiber diameter is used to calculate the surface area per unit length of the sample by assuming a cylindrical rod or tube for core–shell or hollow cases, respectively. From this value, the specific surface area can be calculated by simply dividing the area by the weight of the catalyst. In the case of core–shell sample, the thickness of the ZnO coating should be taken into account. Notably, the change in the specific surface area after thermal treatment is vital in the present context than the absolute value by itself.

2.4. Characterization

The morphologies of the samples were investigated using a scanning electron microscope (SEM, FEI – Quanta 200 FEG). A nominal 5 nm Au/Pd alloy was sputtered onto the samples prior to the SEM imaging. Around 100 fibers were analyzed from the SEM images to estimate the AFD. Transmission electron microscope (TEM, FEI – Tecnai G2 F30) was also employed for the detailed investigation of the hollow samples. For TEM imaging, the samples were dispersed via mild sonication in ethanol and the suspension was collected onto a holey carbon coated TEM grid. Selected area electron diffraction (SAED) patterns were also obtained. X-ray diffraction (XRD) patterns of the ZnO hollow nanofibers were recorded ($2\theta = 30$–$90°$) by employing PANalytical X'Pert Multipurpose X-ray diffractometer with Cu Kα radiation ($\lambda = 0.15418$ nm). The ionic state of the surface elements were determined via X-ray photoelectron spectroscopy (XPS, Thermo Scientific, K-Alpha, monochromatic Al Kα X-ray source, 400 μm spot size, $h\nu = 1486.6$ eV) in the presence of a flood gun charge neutralizer. For the core-level spectra, pass energy and step size were 30 eV and 0.1 eV, respectively. PL measurements were carried
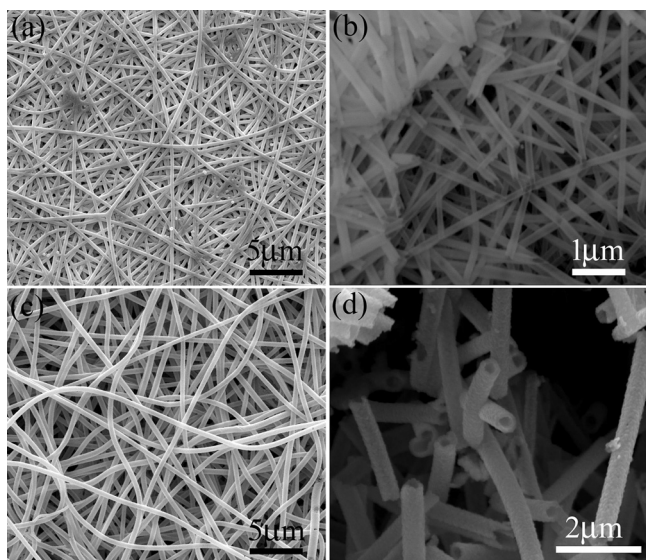
Fig. 2. SEM images of (a) ^{CS}80 nm, (b) ^{H}80 nm, (c) ^{CS}650 nm and (d) ^{H}650 nm. Samples (b) and (d) were intentionally damaged to see the tube-like structure.
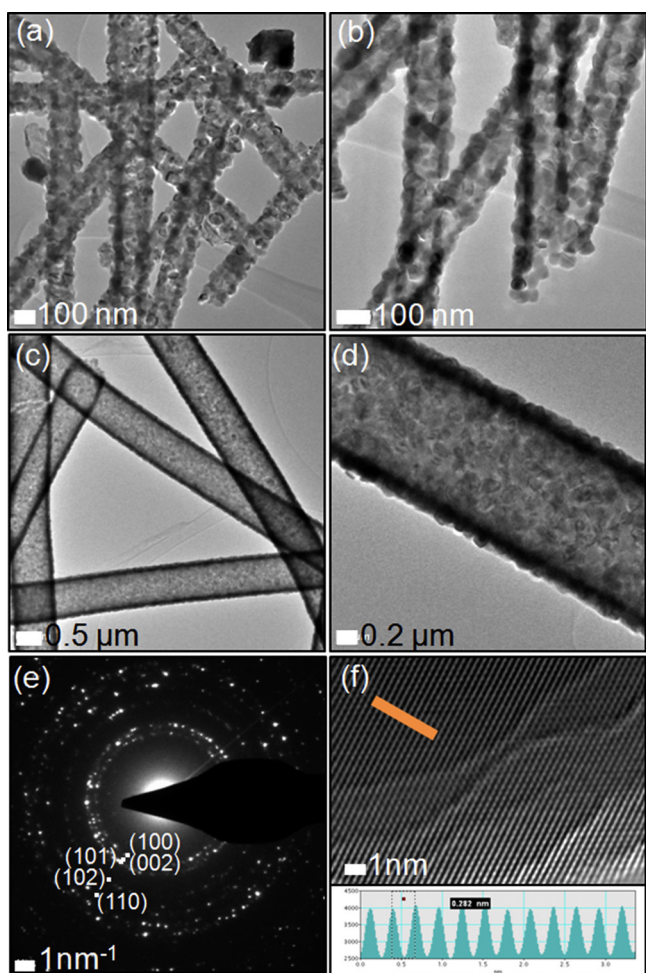

Fig. 3. TEM images of hollow samples. (a), (b) ^{H}80 nm, (c), (d) ^{H}650 nm, (e) SAED pattern from (a), and (f) atomic resolved image showing an interplanar spacing of 0.28 nm.

out using Horiba Scientific FL-1057 TCSPC at an excitation wavelength of ∼360 nm. Peak deconvolutions of the XPS and PL spectra were performed through Avantage and Origin Pro 8.5 softwares, respectively.

2.5. Photocatalytic activity of ZnO hollow nanofibers

The hollow samples (∼5.7 mg each) were immersed individually into quartz cuvettes containing Rh-B aqueous solution (10.4 μM). The cuvettes were exposed to UV light (365 nm, UVLMS-38 EL, 8 W) at a distance of ∼10 cm from the source. The concentration of the dye (intensity of the absorption peak at ∼553 nm) was monitored using an UV–vis–NIR spectrophotometer (Varian Cary 5000) at regular time intervals (t). The catalyst stayed at the bottom of the cuvette during the measurement and did not interfere with the data acquisition. As a control experiment, Rh-B solution without any catalyst was subjected to the same UV treatment in order to compare with the catalyst case. The concentrations of Rh-B before and after UV irradiation were defined as C_0 and C, respectively. The rate of dye degradation (C/C_0) was quantified with first order exponential fit ($y = y_0 + \alpha \, e^{-x/\tau}$) for each sample with an automated routine in Origin Pro8.5 where α-pre exponential factor, x- time axis, y- C/C_0 at different 't' and τ-decay constant. All the parameters are set as free until convergence (unless otherwise stated).

3. Results and discussion

Fig. 1 shows a schematic diagram with various steps involved in producing the core–shell as well as hollow nanofibers. Initially nanofibers were produced with two average diameters which were then subjected to ALD for ZnO coating. The core–shell structure was subjected to calcination yielding hollow nanofibers.

SEM images were recorded on the core–shell and hollow nanofibers and are shown in Fig. 2. We can see the smooth, uniform texture and continuous coating of ZnO. The diameter distributions of pure nylon 6,6 fibers of two different diameters are shown in Fig. S1 of Supporting information. The transformation of surface morphology is convincing by given the fact that the samples were subjected to relatively high temperature thermal treatment. During the thermal treatment the polymer core is decomposed while the inorganic coating (ZnO) is subjected to some changes in its crystallinity. These changes are significant when compared to the hollow samples produced by washing the core [53]. Changes in the crystallinity have significant implications on the optical properties as we will see later in this report. In the context of XRD analysis, the consequence of grainy structure is more explicit for calcined samples compared to as deposited samples. After the calcination (Fig. 2b and d), the tube-like structure evolves from core–shell nanofibers where the samples were slightly broken to observe the hollowness.

TEM images from the hollow samples are shown in Fig. 3. From Fig. 3a–d the tube-like structure is evidenced, apart from the uniform and conformal coating. The tube-like structure is consistent with the SEM observations. Despite of the well developed grains [28], the integral structure of the fiber remains intact for both the cases. Even in the case of ^{H}80 nm sample the grains cover the whole fiber, despite of the average grain size of ∼20 nm. Fig. 3e shows SAED pattern from ^{H}80 nm sample. The pattern shows clear and bright spots suggesting well developed single crystals oriented in various directions. The identified reflections are annotated on the image. In Fig. 3f we have shown atomic resolved image while its insert represent the cross-section analysis. The measured interplanar spacing is ∼0.28 nm which corresponds to the c-axis of ZnO. Wurtzite structure of ZnO can be confirmed from the result of SAED and interplanar spacing [11,18,36,54].
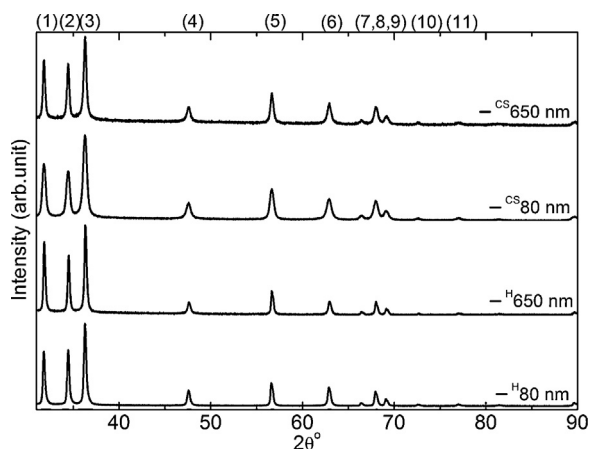
Fig. 4. XRD patterns of core–shell and hollow samples. Reflections enumerated from (1) through (11) are as follows: (100), (002), (101), (102), (110), (103), (200), (112), (201), (004) and (202). XRD data of core–shell samples is taken from Ref. [29].
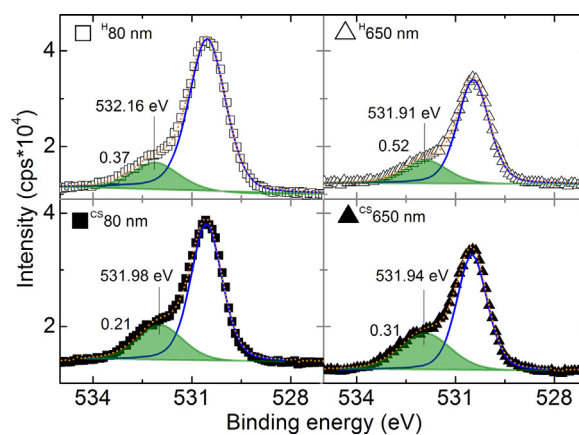

Fig. 5. O1s core-level XPS spectra from core–shell and hollow samples. The fraction of O_{Ch} and its spectral location (in eV) is annotated on the corresponding part.

XRD patterns of core–shell and hollow samples are shown in Fig. 4. Diffraction peaks appeared in the pattern are enumerated from (1) through (11) and listed in the legend of Fig. 4. To understand the effect of calcination on crystallinity, three peaks were selected (1–3, Fig. S2 of Supporting information) and fitted with Lorentizan shape (not shown here). The resultant full width at half maximum (FWHM, δ°) and the lattice parameters are tabulated in Table 1. The angular location of these peaks did not show any significant shift after calcination in the case of 80 nm sample, which suggests the absence of any stress/strain. However, for ^{H}650 nm sample it is slightly shifted to higher 2θ especially for (1 0 0) and (0 0 2) reflections (Fig. S2 of Supporting information), which suggests the existence of a slight residual tensile stress. Also the lattice parameters maintained the c/a ratio of ~1.6. Furthermore, in a broader sense for the three reflections the δ° of sample ^{H}80 nm is seen to decrease by a factor of ~1.5 from their core–shell counterpart. While ^{H}650 nm sample also shown to decrease δ°, however, not as much as the ^{H}80 nm sample. This is understandable, because in the case of 80 nm nanofibers, the relatively lower diameter hinders the growth may be in some specific lattice direction as monolayers are deposited in ALD process in each cycle. Note that the lower diameter is equivalent to higher specific surface area when compared to the substrate with fibers of 650 nm diameter. To compare, δ° with the hollow samples produced by washing the core did not show significant change [53] in contrast to the present samples. When the ^{CS}80 nm sample is subjected to calcination, the polymer core is removed and the lattice spends the gained thermal energy in relaxing and increasing its crystallinity. We mean to refer 'relaxing' in terms of the lowest possible entropic configuration, not angular shift of peaks. XRD patterns from core–shell as well as hollow samples match with the literature and confirm the wurtzite structure [10,18,36,54,55]. Overall, the peaks became sharper as a result of the calcination process, which increased the crystallinity in contrast to the hollow ZnO fibers produced by washing the core [53]. Also the results from XRD corroborate with that of local crystal investigation from TEM.

The surface chemistry is studied by analyzing O1s core-level spectra (Fig. 5). O1s spectrum requires a deeper attention as it is shown [10,11,18] to play a crucial role in the PCA. The spectra shown in Fig. 5 broadly contain two components and one of which is from the oxygen in the ZnO lattice (major peak). Across the four samples, minor-peak at the higher binding energy occurs from the O_{Ch}. However, the origin of O_{Ch} is slightly varying from each other across the samples, see binding energies of O_{Ch} in Fig. 5. It is worth nothing that the O_{Ch} can be from the any of the following species: −OH, −CO, adsorbed H_2O and/or O_2 (Ref. [10,11,18,56]) or O^- and O^{-2} ions [10,11,18]. Area ratios of minor to major peaks suggest the fraction of O_{Ch}. The ratio values are depicted on the image for the corresponding peaks. Among the samples, ^{CS}80 nm has shown the lowest O_{Ch} fraction. Interestingly, after the calcination O_{Ch} fraction is subdued for both cases. The percentage decrease is ~43 and ~40 for 80 nm and 650 nm samples, respectively. It is interesting to note that in the case of hollow samples produced by dissolving the 'core' hosted relatively higher O_{Ch} fraction [53]. The phenomenon of chemisorption of oxygen is complex as it can occupy a variety of places on the surface. In the context of ZnO, for example, oxygen vacancies (V_Os) are prime spots for their adsorption, however, other places such as grain boundaries need to be also taken into account. Essentially after calcination V_Os and grain boundaries are substantially affected due to the changes in the crystallinity (see δ°, Table 1). Note that the analysis of XRD suggested a variation in the FWHM of some reflections. The lattice rearrangement and increased crystallinity are the main reasons for the decreased O_{Ch} component after calcination.

In conjunction with V_Os, optical properties are crucial for PCA of ZnO and/or TiO_2 based catalysts [10,11,18]. PL properties of core–shell and hollow samples are shown in Fig. 6. A clear variation is seen when the core–shell nanofibers are transformed into its hollow counterparts. We have deconvoluted each spectrum and the parameters are tabulated in Table 2 along with the attributed mechanism. However, importantly large intensity variations are noticed across all peaks and we will address them in the latter part of this section.

Table 1
Deconvoluted parameters from XRD analysis.

Sample	FWHM (δ°)			Lattice parameters (Å)	
	(100)	(002)	(101)	(a)	(c)
^{CS}80 nm	0.436	0.436	0.372	3.249	5.206
^{H}80 nm	0.267	0.267	0.267	3.249	5.206
^{CS}650 nm	0.291	0.29	0.327	3.249	5.207
^{H}650 nm	0.249	0.249	0.285	3.245	5.199

Table 2
Spectral locations of deconvoluted peaks (nm) and ascribed emission mechanism for each sample. The spectral location of the peak has a standard error of <1 nm. CB-conduction band, FX-free exciton, Zn_i-zinc interstitials, ex-Zn_i-extended Zn_i states, $V_O{}^*$ neutral oxygen vacancy after electron capture (e_{cptr}) from CB process and $V_O{}^{++}$-doubly positive oxygen vacancy after hole capture (h_{cptr}) from valance band (VB).

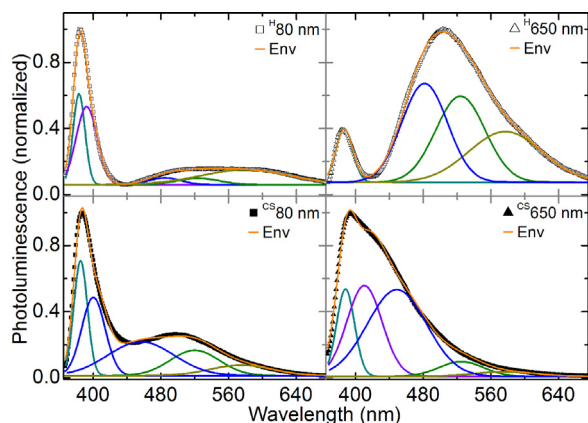| Sample	Interband	V_{Zn}, Zn_i or ex-Zn_i		V_O	
^{CS}80 nm	385	400[1]	457[3]	520	575
^{H}80 nm	383	392[2]	485[4]	523	579
^{CS}650 nm	388	411[1]	448[3]	527	579
^{H}650 nm	387	–	482[4]	520	572
Mechanism	$FX \xrightarrow{395nm} VB$	$^1CB \xrightarrow{405nm} V_{Zn}$ $^2Zn_i \xrightarrow{395nm} VB$	$^3ex\text{-}Zn_i \xrightarrow{440\text{-}455nm} V_{Zn}$ $^4ex\text{-}Zn_i \xrightarrow{492nm} V_{Zn}$	$V_0^* \xrightarrow{524nm} VB$	$CB \xrightarrow{577nm} V_0^{++}$

Fig. 6. Photoluminescence spectra of core–shell and hollow samples of ZnO.

Fig. 7. Schematic band diagram of ZnO with a band gap of 3.3 eV depicting the defects for core–shell and hollow cases. CB-conduction band, FX-free exciton, Zn_i-zinc interstitials, ex-Zn_i-extended Zn_i states, $V_O{}^*$ neutral oxygen vacancy after electron capture (e_{cptr}) from CB and $V_O{}^{++}$-doubly positive oxygen vacancy after hole capture (h_{cptr}) from valance band (VB). For the energetic locations of the various bands, please refer to the cross references in Ref. [36]. The optical transitions were shown (left to right) in an increasing emission wavelength (λ). Refer to Table 2 for the emission wavelengths.
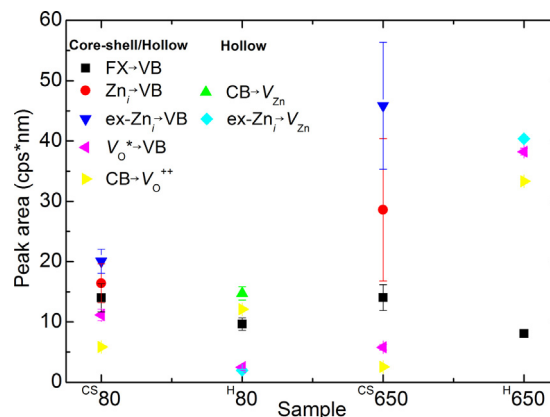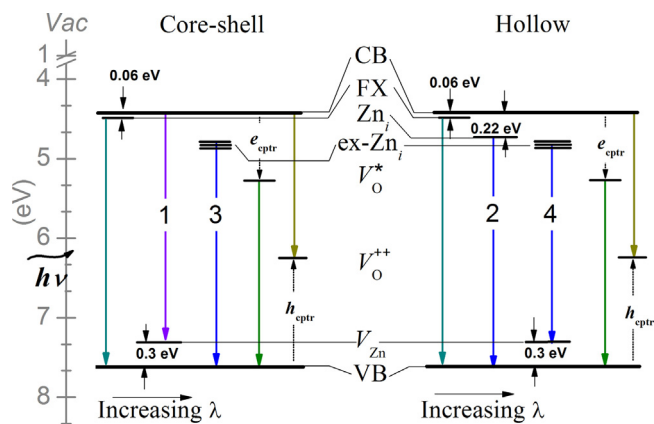

Fig. 8. Area under the curve from each luminescent transition with standard error from the deconvolution. $CB \rightarrow V_{Zn}$ is not observed for ^{H}650 nm sample.

Upon calcination at temperature of about 500 °C, significant changes took place in the lattice apart from the removal of the core-polymer. Reorganization of intrinsic defects (radiative) is an important consequence of this high temperature treatment, which has of course reflected in the PL spectra. 'Reorganization' of defects may consist of variation in density as well as their physical location (localized defects) within the lattice. Since visible emission [36,52,54,55,57–59] and catalysis take place on the surface [12,13], we limit the discussion accordingly. Majorly the present PL spectra consist of V_Os and Zn_is, where striking a balance between them is notably a hard task [50]. However, we have earlier seen the formation of Zn_is in the ALD process on poly(sulfone) nanofibers

because of the differences in the hydrophobicity of the surface functional groups [11]. The intrinsic defects from non-equilibrium process related to oxygen are more stable when compared to those originate from zinc [57–59]. Specifically, Zn_is have a smaller migration barrier of about 0.57 eV, while it is from 1.7 to 2.4 eV for V_Os [59]. On the other hand, the formation temperature determines the relative concentrations of various defects [50]. In the present case, the deposition temperature is ∼200 °C while that of calcination is ∼500 °C which yield energy equivalents of ∼40 and ∼66 meV, respectively. Essentially the defects formed at ∼200 °C are subjected to reorganization at ∼500 °C. In the following, we treat the specifics of each of the defects and the consequences of calcination.

Interesting observations are made for the emissions those were attributed to V_{Zn} or Zn_i. Although it appears to be the case that the band at 450 nm has significantly red-shifted to 483 nm after calcination, however, this shift cannot be explained based on the energetic-shifts of the defect related bands. The energetic locations of the intrinsic defects are characteristics of a material. In fact, after calcination the transition 1 is substituted by 2 and similarly 3 by 4 (Table 2). It is noted that emission 2 is not observed from ^{H}650 nm sample, however, by consulting the emissions 3 and 4, the substitution is convincing.

Refer to the band diagram shown in Fig. 7 for core–shell and hollow cases which schematizes the various transitions shown in Table 2. Note that the substitution (1 by 3 and 2 by 4) compliments each other. By looking at the emission wavelengths and their attributions (except for 4) we can see that Zn_is are formed after calcination, while ex-Zn_is exist in both core–shell and hollow cases. Regarding the emission 4, V_{Zn}s and ex-Zn_is exist before the calcination as well, however, no emission is observed between these two states. This may be because of the fact that they are spatially apart. Calcination has provided a sufficient mobility for the defects to reorganize so that the newly proposed 'transition 4' can take place; i.e., ex-$Zn_i \rightarrow V_{Zn}$. This reorganization has in fact created Zn_is which have shown emission (after calcination, $Zn_i \rightarrow$ VB) in the blue
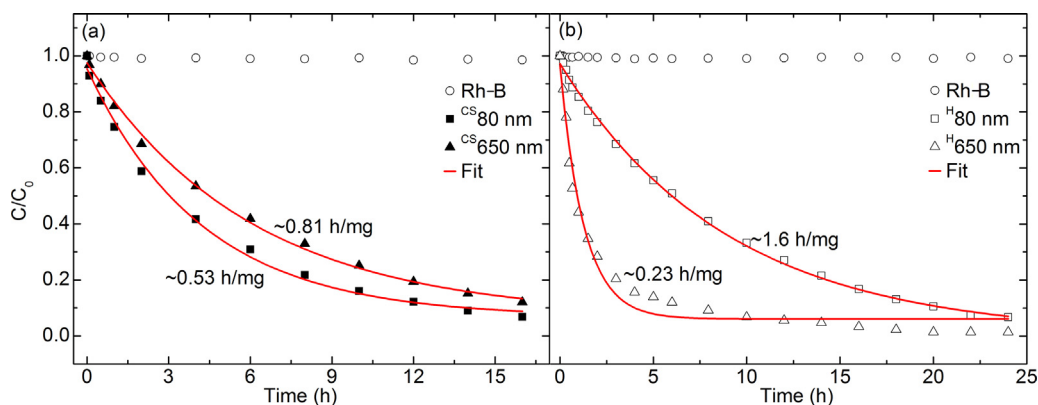
Fig. 9. Photocatalytic activities of (a) core–shell and (b) hollow samples. Data in part (a) is taken from Ref. [29].

region of the spectrum (VB-valance band). Further confirming the attribution for emission 4, the energetic locations match well with the observed emission. ex-Zn_is are 2.82–2.735 eV and V_{Zn} is 0.3 eV above the VB, hence the transition from ex-$Zn_i \to V_{Zn}$ should have emission of about 490 nm, where we noted 482–485 nm (Table 2). Moving onto the other emissions, from Table 2, there is a slight blue shift of the interband transition (FX $\to$ VB) after the calcination may be because of the increased optical quality of the material (FX-free exciton). The emission related to V_Os is almost spectrally invariant by given the typical FWHM of these bands [52].

The relative densities of various defects can be estimated by taking the area under the corresponding peak (Fig. 8) [52]. Before and after the calcination, the areas under each of the transitions are plotted in Fig. 8. To comment on the overall change in the density of the defects, it is seen to decrease after calcination. It is understandable, as the reorganization of defects to their possible lowest entropic state. In the following, we compared each defect density when a transformation took place from core–shell to hollow. To start with, $^{CS}80$ nm sample has lower density of defects than $^{CS}650$ nm sample. FX $\to$ VB emission is slightly decreased for both the samples after calcination. In general, this interband transition subdues under the dominance of defect related emissions which is consistent as the green emission is enhanced. Note that the green emission consists of two components [36,52,55], viz. $V_O^* \to$ VB and CB $\to V_O^{++}$ which occur in bulk and depletion regions respectively (CB-conduction band). We can see that the intensity of $V_O^* \to$ VB decreased in contrast to CB $\to V_O^{++}$ for 80 nm sample after calcination where the latter is increased. On the other hand, both of these emissions were enhanced for 650 nm sample. The grain boundaries and the depletion region are severely altered after the calcination; and hence, an integral effect on the green emission can be expected. Since the emissions 2, 4 and 1, 3 are not seen for core–shell and hollow samples, respectively, we cannot compare the changes in the intensities with respect to calcination.

The basic mechanism of photocatalysis on the surface is the same for any semiconductor catalyst; however, the density of defects and their accessibility to the dye determine the time constant of the process. Please refer to our previous articles in which PCA is elaborately discussed in the context of various defects of ZnO [10,11,18]. Note that the actual mechanism is initially discussed by Matthews [13] and Hoffmann et al. [12]. In order to quantitatively compare the PCA of core–shell and hollow samples, the decay constants (from the exponential fit) are normalized to the corresponding weight of the catalyst and shown on Fig. 9. This normalized rate constant is a very good measure of the catalytic activity where the lower value suggests better catalytic activity. Thermogravimetric analysis is employed to extract the weight [29] of the ZnO from the core–shell catalyst. The decay constants from

core–shell and hollow samples in an increasing order are as follows: $^H650 < {}^{CS}80 < {}^{CS}650 < {}^H80$. Although $^H80$ nm sample has the highest theoretical specific surface area, the surface defects play a crucial role in determining the PCA. It is known that relatively higher density of defects exhibit high PCA [10,11,18]. In order to estimate the density of defects, we employ the results from the PL data and peak deconvolution therein. The overall density of defects (sum of the area under the peaks related to defects, Fig. 8) for four samples is in the following decreasing order: $^H650 > {}^{CS}650 > {}^{CS}80 > {}^H80$. Although it appears that there is a slight disagreement in the order of the time constant and the overall density of defects, still the results are consistent as the standard error in the peak fitting is relatively higher for $^{CS}650$ nm sample. While calculating the overall defect density, the green component, $V_O^* \to$ VB transition is also included. Despite, this transition occurs in the bulk of the grain [10,11,18,52], it helps the PCA process indirectly by delaying the recombination [12,13]. This is the case with any of the defects; if they are on the surface then electron and hole take part in PCA before they recombine [10–13,18].

4. Conclusions

We have systematically compared the PCA of two different diameters of nanofiber catalysts in core–shell and hollow forms produced via combining electrospinning and ALD. These catalysts were thoroughly characterized for their morphological, structural, surface and optical properties. Sharpening of the XRD peaks is observed after calcination suggesting an improved crystal quality. The fraction of O_{Ch} is decreased ~43% and ~40% for $^H80$ nm and $^H650$ nm after calcination, respectively. Interestingly, from the PL data a new emission (ex-$Zn_i \to V_{Zn}$) is proposed which is supported by the simulated emission wavelength against the energetic locations of the intrinsic defects within the band gap. This new emission is explained based on the reorganization of the intrinsic defects during the thermal treatment. Since these defects are localized within the lattice, the thermal energy has in fact allowed the spatial redistribution. The total density of defects was analyzed in conjunction with the PCA for each of the samples. The results suggested that in the case of ZnO samples enhancing the specific surface area does not necessarily increase the PCA.

F. Kayaci et al. / Applied Catalysis B: Environmental 176–177 (2015) 646–653

Award Program (TUBA-GEBIP) for partial funding. Authors thank M. Guler for technical support for TEM analysis.

Appendix A. Supplementary data

Supplementary data associated with this article can be found, in the online version, at http://dx.doi.org/10.1016/j.apcatb.2015.04.036.

References

[1] Z. Li, S. Cong, Y. Xu, Brookite vs anatase TiO$_2$ in the photocatalytic activity for organic degradation in water, ACS Catal. 4 (2014) 3273–3280.
[2] I.E. Wachs, S.P. Phivilay, C.A. Roberts, Reporting of reactivity for heterogeneous photocatalysis, ACS Catal. 3 (2013) 2606–2611.
[3] Y. Shiraishi, Y. Togawa, D. Tsukamoto, S. Tanaka, T. Hirai, Highly efficient and selective hydrogenation of nitroaromatics on photoactivated rutile titanium dioxide, ACS Catal. 2 (2012) 2475–2481.
[4] B.K. Vijayan, N.M. Dimitrijevic, D.F. Shapiro, J. Wu, K.A. Gray, Coupling titania nanotubes and carbon nanotubes to create photocatalytic nanocomposites, ACS Catal. 2 (2011) 223–229.
[5] Y. Shiraishi, H. Hirakawa, Y. Togawa, T. Hirai, Noble-metal-free deoxygenation of epoxides: titanium dioxide as a photocatalytically regenerable electron-transfer catalyst, ACS Catal. 4 (2014) 1642–1649.
[6] M. Xing, W. Fang, X. Yang, B. Tian, J. Zhang, Highly-dispersed boron-doped graphene nanoribbons with enhanced conductibility and photocatalysis, Chem. Commun. 50 (2014) 6637–6640.
[7] W. Gao, M. Wang, C. Ran, X. Yao, H. Yang, J. Liu, D. He, J. Bai, One-pot synthesis of Ag/r-GO/TiO$_2$ nanocomposites with high solar absorption and enhanced anti-recombination in photocatalytic applications, Nanoscale 6 (2014) 5498–5508.
[8] S. Kumar, A. Baruah, S. Tonda, B. Kumar, V. Shanker, B. Sreedhar, Cost-effective and eco-friendly synthesis of novel and stable N-doped ZnO/g-C$_3$N$_4$ core–shell nanoplates with excellent visible-light responsive photocatalysis, Nanoscale 6 (2014) 4830–4842.
[9] F. Dong, T. Xiong, Y. Sun, Z. Zhao, Y. Zhou, X. Feng, Z. Wu, A semimetal bismuth element as a direct plasmonic photocatalyst, Chem. Commun. 50 (2014) 10386–10389.
[10] F. Kayaci, S. Vempati, C. Ozgit, I. Donmez, N. Biyikli, T. Uyar, Selective isolation of electron or hole in photocatalysis: ZnO-TiO$_2$ and TiO$_2$-ZnO core–shell structured heterojunction nanofibers via electrospinning and atomic layer deposition, Nanoscale 6 (2014) 5735.
[11] F. Kayaci, S. Vempati, I. Donmez, N. Biyikli, T. Uyar, Role of zinc interstitials and oxygen vacancies of ZnO in photocatalysis: a bottom-up approach to control defect density, Nanoscale 6 (2014) 10224–10234.
[12] M.R. Hoffmann, S.T. Martin, W. Choi, D. Bahnemann, Environmental applications of semiconductor photocatalysis, Chem. Rev. 95 (1995) 69–96.
[13] R.W. Matthews, Photocatalytic oxidation of chlorobenzene in aqueous suspensions of titanium dioxide, J. Catal. 97 (1986) 565–568.
[14] I. Izumi, W.W. Dunn, K.O. Wilbourn, F.R.F. Fan, A.J. Bard, Heterogeneous photocatalytic oxidation of hydrocarbons on platinized TiO$_2$ powders, J. Phys. Chem. 84 (1980) 3207–3210.
[15] N. Zhang, Y.-J. Xu, Aggregation- and leaching-resistant, reusable, and multifunctional Pd@CeO$_2$ as a robust nanocatalyst achieved by a hollow core–shell strategy, Chem. Mater. 25 (2013) 1979–1988.
[16] N. Zhang, S. Liu, Y.-J. Xu, Recent progress on metal core@semiconductor shell nanocomposites as a promising type of photocatalyst, Nanoscale 4 (2012) 2227–2238.
[17] C. Yu, K. Yang, Y. Xie, Q. Fan, J.C. Yu, Q. Shu, C. Wang, Novel hollow Pt-ZnO nanocomposite microspheres with hierarchical structure and enhanced photocatalytic activity and stability, Nanoscale 5 (2013) 2142–2151.
[18] F. Kayaci, S. Vempati, N. -Akgun, T. Uyar, Enhanced photocatalytic activity of homoassembled ZnO nanostructures on electrospun polymeric nanofibres: a combination of atomic layer deposition and hydrothermal growth, Appl. Catal. B 156–157 (2014) 173–183.
[19] H. Tada, T. Kiyonaga, S. Naya, Rational design and applications of highly efficient reaction systems photocatalyzed by noble metal nanoparticle-loaded titanium(IV) dioxide, Chem. Soc. Rev. 38 (2009) 1849–1858.
[20] I. Nakamura, N. Negishi, S. Kutsuna, T. Ihara, S. Sugihara, K. Takeuchi, Role of oxygen vacancy in the plasma-treated TiO$_2$ photocatalyst with visible light activity for NO removal, J. Mol. Catal. A 161 (2000) 205–212.
[21] X.M.-Q. Pan Yang, X. Fu, N. Zhang, Y.-J. Xu, Defective TiO$_2$ with oxygen vacancies: synthesis, properties and photocatalytic applications, Nanoscale 5 (2013) 3601–3614.
[22] M.K. Nowotny, L.R. Sheppard, T. Bak, J. Nowotny, Defect chemistry of titanium dioxide. Application for defect engineering in processing of TiO$_2$-based photocatalysts, J. Phys. Chem. C 112 (2008) 5275.
[23] J. Wang, P. Liu, X. Fu, Z. Li, W. Han, X. Wang, Relationship between oxygen defects and the photocatalytic property of ZnO nanocrystals in Nafion membranes, Langmuir 25 (2008) 1218–1223.
[24] C. Yu, G. Li, S. Kumar, K. Yang, R. Jin, Phase transformation synthesis of novel Ag$_2$O/Ag$_2$CO$_3$ heterostructures with high visible light efficiency in photocatalytic degradation of pollutants, Adv. Mater. 26 (2013) 892–898.
[25] Y. Zhang, Z.-R. Tang, X. Fu, Y.-J. Xu, TiO$_2$- graphene nanocomposites for gas-phase photocatalytic degradation of volatile aromatic pollutant: is TiO$_2$– graphene truly different from other TiO$_2$– carbon composite materials? ACS Nano 4 (2010) 7303–7314.
[26] M.-Q. Yang, N. Zhang, M. Pagliaro, Y.-J. Xu, Artificial photosynthesis over graphene – semiconductor composites. Are we getting better? Chem. Soc. Rev. 43 (2014) 8240–8254.
[27] F. Xu, Y. Shen, L. Sun, H. Zeng, Y. Lu, Enhanced photocatalytic activity of hierarchical ZnO nanoplate–nanowire architecture as environmentally safe and facilely recyclable photocatalyst, Nanoscale 3 (2011) 5020–5025.
[28] F. Kayaci, C. Ozgit-Akgun, N. Biyikli, T. Uyar, Surface-decorated ZnO nanoparticles and ZnO nanocoating on electrospun polymeric nanofibers by atomic layer deposition for flexible photocatalytic nanofibrous membranes, RSC Adv. 3 (2013) 6817–6820.
[29] F. Kayaci, C. Ozgit-Akgun, I. Donmez, N. Biyikli, T. Uyar, Polymer–inoganic core–shell nanofibers by electrospinning and atomic layer deposition: flexible nylon–ZnO core–shell nanofiber mats and their photocatalytic activity, ACS Appl. Mater. Interfaces 4 (2012) 6185–6194.
[30] H. Liu, J. Yang, J. Liang, Y. Huang, C. Tang, ZnO nanofiber and nanoparticle synthesized through electrospinning and their photocatalytic activity under visible light, J. Am. Ceram. Soc. 91 (2008) 1287–1291.
[31] A. Sugunan, V.K. Guduru, A. Uheida, M.S. Toprak, M. Muhammed, Radially oriented ZnO nanowires on flexible poly-L-lactide nanofibers for continuous-flow photocatalytic water purification, J. Am. Ceram. Soc. 93 (2010) 3740–3744.
[32] N. Zhang, Y. Zhang, Y.-J. Xu, Recent progress on graphene-based photocatalyst: current status and future perspectives, Nanoscale 4 (2012) 5792.
[33] Z. Chen, N. Zhang, Y.-J. Xu, Synthesis of graphene–ZnO nanorod nanocomposites with improved photoactivity and anti-photocorrosion, CrystEngComm 15 (2013) 3022–3030.
[34] C. Han, M.-Q. Yang, B. Weng, Y.-J. Xu, Improving the photocatalytic activity and anti-photocorrosion of semiconductor ZnO by coupling with versatile carbon, Phys. Chem. Chem. Phys. 16 (2014) 16891–16903.
[35] S. Vempati, Y. Ertas, T. Uyar, Sensitive surface states and their passivation mechanism in cds quantum dots, J. Phys. Chem. C 117 (2013) 21609–21618.
[36] S. Vempati, J. Mitra, P. Dawson, One-step synthesis of ZnO nanosheets: a blue–white fluorophore, Nanoscale Res. Lett. 7 (2012) 470.
[37] U. Ozgur, Y. Alivov, C. Liu, A. Teke, M. Reshchikov, S. Dogan, V. Avrutin, S. Cho, H. Morkoc, A comprehensive review of ZnO materials and devices, J. Appl. Phys. 98 (2005) 041301.
[38] L. Schmide-Mende, J.L. MacManus-Driscoll, ZnO-nanostructures, defects, and devices, Mater. Today 10 (2007) 40.
[39] T.J. Athauda, P. Hari, R.R. Ozer, Tuning physical and optical properties of ZnO nanowire arrays grown on cotton fibers, ACS Appl. Mater. Interfaces 5 (2013) 6237–6246.
[40] C.J. Oldham, B. Gong, J.C. Spagnola, J.S. Jur, K.J. Senecal, T.A. Godfrey, G.N. Parsons, Encapsulation and chemical resistance of electrospun nylon nanofibers coated using integrated atomic and molecular layer deposition, J. Electrochem. Soc. 158 (2011) D549–D556.
[41] T.J. Athauda, U. Butt, R.R. Ozer, One-dimensional hierarchical composite materials based on ZnO nanowires and electrospun blend nanofibers, RSC Adv. 3 (2013) 21431–21438.
[42] A. Celebioglu, T. Uyar, Electrospinning of nanofibers from non-polymeric systems: polymer-free nanofibers from cyclodextrin derivatives, Nanoscale 4 (2012) 621–631.
[43] S. Ramakrishna, K. Fujihara, W. Teo, T. Lim, Z. Ma, An Introduction to Electrospinning and Nanofibers, World Scientific Publishing Company, Singapore, 2005.
[44] T. Uyar, Y. Nur, J. Hacaloglu, F. Besenbacher, Electrospinning of functional poly(methyl methacrylate) nanofibers containing cyclodextrin–menthol inclusion complexes, Nanotechnology 20 (2009) 125703.
[45] C. Ozgit-Akgun, F. Kayaci, I. Donmez, T. Uyar, N. Biyikli, Template-based synthesis of AlN hollow nanofibers via plasma-enhanced atomic layer deposition, J. Am. Ceram. Soc. 96 (2013) 916–922.
[46] I. Donmez, F. Kayaci, C. Ozgit-Akgun, T. Uyar, N. Biyikli, Fabrication of hafnia hollow nanofibers by atomic layer deposition using electrospun nanofiber templates, J. Alloys Compd. 559 (2013) 146–151.
[47] E. Santala, M. Kemmel, M. Leskela, M. Ritala, The preparation of reusable magnetic and photocatalytic composite nanofibers by electrospinning and atomic layer deposition, Nanotechnology 20 (2009) 035602.
[48] W.J. Sweet, J.S. Jur, G.N. Parsons, Bi-layer Al$_2$O$_3$/ZnO atomic layer deposition for controllable conductive coatings on polypropylene nonwoven fiber mats, J. Appl. Phys. 113 (2013) 194303.
[49] J.S. Jur, W.J. Sweet III, C.J. Oldham, G.N. Parsons, Atomic layer deposition of conductive coatings on cotton, paper, and synthetic fibers: conductivity analysis and functional chemical sensing using all-fiber capacitors, Adv. Funct. Mater. 21 (2011) 1993–2002.
[50] H. Zeng, G. Duan, Y. Li, S. Yang, X. Xu, W. Cai, Blue luminescence of ZnO nanoparticles based on non-equilibrium processes: defect origins and emission, Adv. Funct. Mater. 20 (2010) 561.
[51] J.D. Ye, S.L. Gu, F. Qin, S.M. Zhu, S.M. Liu, X. Zhou, W. Liu, L.Q. Hu, R. Zhang, Y. Shi, Y.D. Zheng, Correlation between green luminescence and morphology evolution of ZnO films, Appl. Phys. A: Mater. Sci. Process. 81 (2005) 759–762.

[52] S. Vempati, S. Chirakkara, J. Mitra, P. Dawson, K.K. Nanda, S.B. Krupanidhi, Unusual photoresponse of indium doped ZnO/organic thin film heterojunction, Appl. Phys. Lett. 100 (2012) 162104.

[53] A. Celebioglu, S. Vempati, C. Ozgit-Akgun, N. Biyikli, T. Uyar, Water-soluble non-polymeric electrospun cyclodextrin nanofiber template for the synthesis of metal oxide tubes by atomic layer deposition, RSC Adv. 4 (2014) 61698–61705.

[54] S. Vempati, A. Shetty, P. Dawson, K.K. Nanda, S.B. Krupanidhi, Solution-based synthesis of cobalt-doped ZnO thin films, Thin Solid Films 524 (2012) 137–143.

[55] S. Vempati, A. Shetty, P. Dawson, K. Nanda, S.B. Krupanidhi, Cobalt-doped ZnO nanowires on quartz: Synthesis by simple chemical method and characterization, J. Cryst. Growth 343 (2012) 7–12.

[56] A. Stănoiu, C.E. Simion, S. Somăcescu, NO2 sensing mechanism of ZnO–Eu_2O_3 binary oxide under humid air conditions, Sens. Actuators B: Chem. 186 (2013) 687–694.

[57] V. Ischenko, S. Polarz, D. Grote, V. Stavarache, K. Fink, M. Driess, Zinc oxide nanoparticles with defects, Adv. Funct. Mater. 15 (2005) 1945.

[58] L.S. Vlasenko, G.D. Watkins, Optical detection of electron paramagnetic resonance for intrinsic defects produced in ZnO by 2.5-MeV electron irradiation in situ at 4.2 K, Phys. Rev. B 72 (2005) 035203.

[59] A. Janotti, C.G. Van de Walle, Native point defects in ZnO, Phys. Rev. B 76 (2007) 165202.